Chemical Engineering Journal Advances 8 (2021) 100166

Contents lists available at ScienceDirect

Chemical Engineering Journal Advances

journal homepage: www.sciencedirect.com/journal/chemical-engineering-journal-advances

Infrared thermospectroscopic imaging of heat and mass transfers in laminar microfluidic reactive flows

S. Chevalier [a,*], J.-N. Tourvieille [b], A. Sommier [a], C. Pradère [a,b]

[a] I2M UMR 5295, Arts et Metiers Institute of Technology, University of Bordeaux, CNRS, Bordeaux INP, INRAE, Bâtiment A11, 351 Cours de la Libération 33405 Talence, France
[b] Solvay, Laboratoire du Futur, CNRS UMR 5258, 178, avenue du Docteur Schweitzer, Pessac 33608, France

ARTICLE INFO

Keywords:
Thermospectroscopy
Microfluidic reactor
FTIR imaging
Inverse processing
Thermal fields
Heat and mass transfer

ABSTRACT

In this work, a novel image-based method is presented to characterize the heat and mass transfer rates in a Hele-Shaw microfluidic reactor. A Fourier transform infrared (FTIR) spectrometer is used in transmission mode in combination with an infrared (IR) camera to simultaneously measure the molar concentration and the thermal fields in the microfluidic chip within few seconds. A classical exothermic NaOH + HCl → NaCl + H_2O chemical reaction is used to produce a multiphase flow and a heat source in the reactor. The molar concentration fields of all the species are measured using the IR spectrum in the mid-IR region, and the heat fields are obtained simultaneously from the proper emission. The quantitative aspect of the method is illustrated by comparing the molar concentration profiles to a reactor model, based on the advection-diffusion-reaction equations. The good agreement between the model and experimental data validates the method, and the expected strong diffusion-limited reaction regime in laminar microfluidic reactor is achieved. Thus, the results of this work provide a new and efficient thermospectroscopic imaging method to perform rapid, contactless and in operando heat and mass transfer characterizations in laminar microfluidic reactive flows.

1. Introduction

Over the past twenty years, microfluidic reactors have revolutionized the chemist's toolkit from round-bottomed flasks to square centimeter lab on chips [1,2]. Because they enable the control and the characterization of physicochemical processes at the microscale, they are used in a wide range of applications from biology [2,3], analytical chemistry [4,5], to nanoparticle production [6,7] among others. In many of those applications, there is a strong need for the knowledge and for modeling the chemical reactions that take place inside the reactors [8]. For example, hydrodynamics, mass transfer [9], and heat release [10] are all parameters that can modify the reactor performances. Decoupling all these parameters is then required to assess physico-chemical properties accurately. In addition, the rapid development of artificial intelligence and machine learning algorithm needs to produce a large quantity of data related to all the physicochemical processes [11]. In particular, temperature field measurements in microfluidic chips are not systematically performed although numerous chemical reactions involve non isothermal flows, even in laminar microfluidic channels. Thus, this context calls for the development of new, online and contactless methods for analytical chemistry, which this work aims to answer with a novel image-based method to measure in operando molar concentrations fields and the heat and mass transfer rates in a microfluidic reactor.

There are several different experimental techniques to investigate the physical processes occurring in microfluidics chips. Imaging methods involving fluorescence microscopy [12–15] were widely used. These methods enable a spatial resolution down to 10 μm but have the disadvantage of being limited to a specific set of molecules that can be linked to a fluorophore. These techniques also require calibration to link the fluorescence intensity to the molar concentration, and in general only one compound of many species in the solution will be tracked [14,15]. To improve this, spectroscopic techniques have been also used. Among them, Raman imaging appears to be one great alternative technique for measuring the molar concentration of different species in solution as this technique gives a specific spectral signature for each compound. Salmon et al. [16] used Raman spectroscopy to identify the spectral signature of each species and they were able to measure the molar fraction fields and to estimate the mass diffusivity. Several other image-based characterization studies of microfluidic chip used a similar

* Corresponding author.
E-mail address: stephane.chevalier@u-bordeaux.fr (S. Chevalier).

https://doi.org/10.1016/j.ceja.2021.100166
Received 29 April 2021; Received in revised form 20 July 2021; Accepted 10 August 2021
Available online 13 August 2021

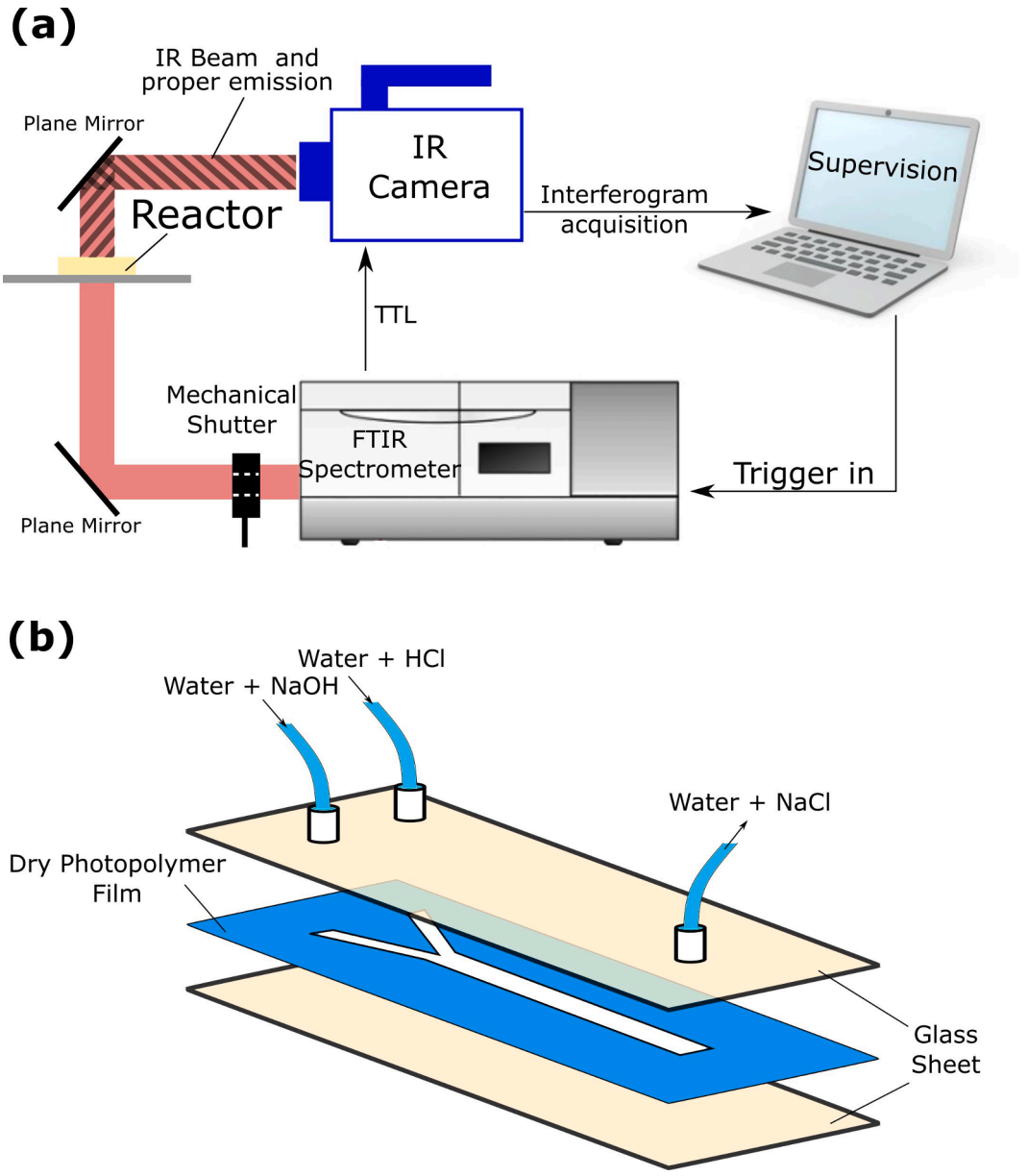

Fig. 1. Experimental setup. (a) The thermospectroscopic platform. (b) Schematic of the microfluidic reactor used to produce the acid/base reaction.

approach [17,18]. However, this technique suffers from a low temporal resolution, i.e. it is a point by point measurement and a complete image requires about hour to be recorded [16], which is not compatible with an online characterization process. Moreover, with this Raman technique, it is not possible to access the temperature parameter. In the case of reactive flow, it is a very important parameter as the mixing does not always lead to isothermal flow due to the large reaction enthalpy of some species.

In this context, infrared (IR) spectroscopic techniques were developed in the last twenty years. Image-based Fourier transform infrared (FTIR) spectroscopy in microfluidics was first used by Hinsmann et al. [5] using a single IR sensor. Many works followed with great improvements in terms of spatial, temporal and spectral resolution [19,20], notably the first works of Chan et al. and their development on FTIR imaging [21]. An exhaustive review summarizing all these recent works can be found in Ref. [22]. The main advantage of IR spectroscopic techniques relies on its ability to measure the molar concentration of each species from the multispectral absorbance using the Beer-Lambert law [23,24]. For example, in their work, Uema et al. [25] were able to measure the molar concentration in aqueous acid–base reactions. To achieve such result, the authors used a delicate calibration of the species absorbance at three wavelengths prior to their measurement, but according to these authors, the choice of only three wavelengths hinder the accuracy of the molar concentration measurements, and the use of advanced spectroscopic method (based on FTIR for example) would be advised. In the work of Ryu et al. [20], a thermospectroscopic measurement of the styrene radical polymerization in a microfluidic channel was performed using a monochromator in combination with an IR camera. The authors reported the simultaneous measurements of concentration and temperature fields at the microscale, but no quantitative processing was done to obtain the physical properties of the reactions. Thus, following these works [20,25], it appears that both the accuracy of the thermospectroscopic imaging method via the use of a FTIR spectrometers, and a thorough processing of the data via an analytical inverse method based on advection-reaction-diffusion model to extract the physical properties of the chemical reactions would lead to significant improvement.

The previous literature review claims for the development of a new

experimental technique which would enable the fast in operando characterization all the species in solution as well as the heat and molar concentration fields. This data would be of great interest to understand the role of physical parameters in the reaction (diffusivity, reaction rates…) and how they impact the chemical reaction itself and/or the quality of the final products. The present study answers this need by providing a FTIR thermospectroscopic image-based technique to image the heat and molar concentration fields of all the species in a microfluidic reactor. To validate the quantitative aspect of the method, the mass transport and transfer rate of the sodium hydroxide reacting with hydrochloric acid are characterized in the diffusion-limited regime [26]. The comparison of the molar concentration profiles to a reactor model reveals a transfer rate in the order of 100 ms (compared to the intrinsic one which is in the order of 1 ns) evidencing the presence of the so-called diffusion-limited mass transport rate. To demonstrate this result, the present paper describes the experimental method and the reactor model in Section 2. Then, the measurements of the molar concentration, mass transport and mass transfer rates are presented, and discussed in Section 3.

2. Methodology

Subsequently, the species NaOH, HCl and NaCl are designated by the subscripts *A, B* and *C*, respectively.

2.1. Experimental setup

2.1.1. Multispectral absorbance measurements

A spectroscopic imaging platform was developed in house to measure the in operando concentration fields in microfluidic reactors [27, 28]. This platform comprises a commercial FTIR spectrometer (Thermo Scientific Nicolet S50R) and a FLIR SC7000 InSb mid-IR camera (spectral range 2.5–6 μm) to measure the sample multispectral 2D absorbance fields in the mid IR region. This spectral region is interesting when working with aqueous solutions, as water is relatively transparent in this domain.

The IR beam is collimated inside the spectrometer, and beam expanded using a homemade system of parabolic mirror. It leads to a beam with an approximate diameter of 4 cm. A schematic of the experimental setup is presented in Fig. 1(a), and the full data processing is detailed in Ref. [27]. The whole area of the microfluidic reactor is imaged using this setup (60 by 360 px) with a spatial resolution of 83 μm/px.

The chemical reaction of $NaOH + HCl \rightarrow NaCl + H_2O$ takes place in a Hele-Shaw *T*-junction microfluidic reactor as depicted in Fig. 1(b). Such geometry was shown to be optimal for diffusion and reaction characterization [15]. The reactor is made of a punched *Y*-shape microchannel of 3 cm by 5 mm in 100 μm-thick LAMINAR® E9012 dry film photopolymer. Thus, this microfluidic channel has an optical path of 100 μm. The *Y*-shape pattern is reproduced in the film with an automated cutter (Graphtec Craft Robo Pro). This thin film is sandwiched between two glass sheets (Menzel-Glaser) that are semi-transparent to IR in the mid-IR range (around 50% of absorption). Sodium hydroxide (Fisher Scientific, 0.5 mol/l) and hydrochloric acid (Fisher Scientific, 0.5 mol/l) are injected in the chip with a NEMESYS Cetoni syringe pump, from each branch of the *Y*-shape channel in order to have a laminar co-flow. The reaction of 0.5 mol/l of NaOH and HCl produces 0.25 mol/l of NaCl with H_2O as a by-product of the reaction.

For each flow rate, three IR interferograms were recorded with a 4 cm^{-1} spectral resolution. The spectrometer optical velocity was set to 0.0633 cm/s, and the IR camera frame rate to 370 Hz. With these setup parameters, a complete interferogram field was imaged every 8 s. These interferograms were then processed to IR spectra and averaged. Three background interferograms made of an empty reactor were also recorded, processed to IR spectra and averaged. The measurements of the background interferograms avoid the influence of the reactor housing in the spectroscopic measurements. With this current setup and camera configuration, the whole spectral range from 1600 to 3000 cm^{-1} (3.3 to 5.5 μm) was imaged. Finally, a multispectral absorbance field was obtained for each flow rate from the decimal logarithm ratio of the sample spectrum to the background spectrum.

2.1.2. Reactants and product concentration measurements

The objective is to convert the multispectral absorbance fields into reactant and product concentration fields. Using the Beer-Lambert law, it is possible to link the absorbance to the concentration as

$$A(\nu) = \sum_i \mu_i(\nu) c_i, \tag{1}$$

where $A(\nu)$ is the multispectral absorbance measured,μ is the absorptivity coefficient (l/mol), ν is the wavenumber (cm^{-1}), and c_i is the molar concentration (mol/l) of the species *i*. The optical path length (100 μm) is included into the value of μ. From Eq. (1), the molar concentration can be measured [29] if the multispectral absorptivity coefficient, $\mu(\nu)$, of each species in solution is known. It is also assumed that the temperature has no influence on the value of $\mu(\nu)$ or c_i as long as the temperature increase is kept relatively low (i.e. lower than 10 K). [25]

Using the mass conservation in the NaOH/HCl reaction leads to $c_0 = c_A + c_B + 2c_C$ where c_0 is the total concentration, i.e. $c_0 = 0.5$ mol/l. The water molecule produced during the reaction contributes to decrease the concentration of NaCl and therefore change the absorbance measured. Thus, the mass conservation relation enables to rewrite Eq. (1) as:

$$2A(\nu) - \mu_C(\nu)c_0 = (2\mu_A(\nu) - \mu_C(\nu))c_A + (2\mu_B(\nu) - \mu_C(\nu))c_B. \tag{2}$$

Using a matrix formalism, one can write that:

$$\begin{pmatrix} 2A^{\nu_1} - \mu_C^{\nu_1} c_0 \\ \vdots \\ 2A^{\nu_N} - \mu_C^{\nu_N} c_0 \end{pmatrix} = \begin{bmatrix} 2\mu_A^{\nu_1} - \mu_C^{\nu_1} & 2\mu_B^{\nu_1} - \mu_C^{\nu_1} \\ \vdots & \vdots \\ 2\mu_A^{\nu_N} - \mu_C^{\nu_N} & 2\mu_B^{\nu_N} - \mu_C^{\nu_N} \end{bmatrix} \begin{pmatrix} c_A \\ c_B \end{pmatrix} \Leftrightarrow A = \mu C, \tag{3}$$

where bold letters designate vectors or matrices. Using a Gauss-Markov inverse method, one can deduce the concentration vector from the absorbance vector as $C = [\mu^T\mu]^{-1}\mu^T A$. This equation is used at each pixel of the image to transform the multispectral absorbance fields into concentration fields (one image per species). The NaOH and HCl concentrations are obtained from the vector *C*, and the NaCl concentration is obtained from the mass conservation as $c_C = \frac{1}{2}(c_0 - c_A - c_B)$. This method is presented for the three species here, but it can be extended to *N* species following the exact same methodology as long as the absorption coefficients of each species are known and each presents different spectral signatures.

2.1.3. Temperature field measurements

The heat fields are measured when the beam from the spectrometer is switched off by closing the mechanical shutter, see Fig. 1(a). In this case, the IR camera measures only the proper emission from the microfluidic chip. The camera was calibrated prior to the measurements with a black body to convert the sample proper emission in temperature. This calibration can be used to measure the temperature fields if the emissivity,ε, of the sample is known.

In case of highly absorbent samples, i.e. transmittance close to 0, and by assuming that the thermal equilibrium is reached and there is no reflection on the sample (reflectivity close to 0), one can demonstrate, according to the Kirchhoff law, that the absorptivity is equal to the emissivity, so $\varepsilon \approx 1 - \Gamma$,where $\Gamma = I/I_0$ is the IR transmittance in the sample, I is the transmitted signal and I_0 is the background signal. Therefore, as the transmittance in the microfluidic flow studied in this paper is close to 0, it can be deduced that $\varepsilon \approx 1$, and the calibration curve of the IR camera can be used to convert the microfluidic proper emission to temperature with the assumption that the proper emission from the chip is close to the black body. The uncertainty in temperature

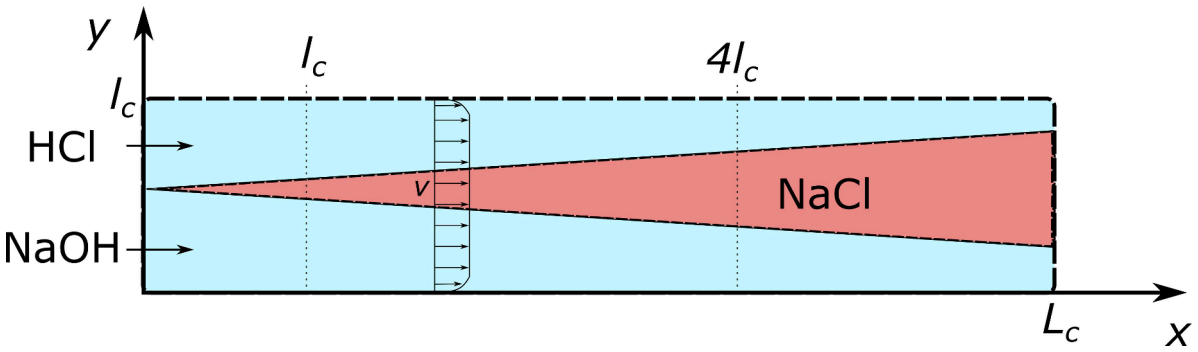

Fig. 2. Schematic of the chemical reaction in the microfluidic Hele Shaw reactor. Most of the processing in the results and discussion section are done at the position l_c and $4l_c$.

measurements is estimated to be around 0.1 K.

The temperature fields measured in this study are only relative temperature. To do so, the background temperature fields, taken prior to flow the reactants through the chip, was subtracted to the temperature fields imaged during the experiments. These measurements were performed simultaneously after each IR spectrum measurements [27], and for all the flow rates studied in this paper. Each heat fields presented in the paper results from the average of 500 images taken in about 3 s.

2.2. Reactor model

2.2.1. General equations

We consider a Hele-Shaw flow in a microfluidic channel with a width $l_c = 5$ mm and a length $L_C = 6l_c = 30$ mm. The channel thickness, $h_c = 0.1$ mm, is assumed to be small enough to ensure that the aspect ratio $h_c/l_c \ll 1$. At the channel inlet, hydrochloric acid and sodium hydroxide are injected as depicted in Fig. 2. The chemical reaction of these reactant leads to the production of sodium chloride and water which creates a diffusion cone that diffuses in the y-direction.

The general steady-state advection-reaction-diffusion equation describing the distribution of species molar concentrations in a 2D channel is [14]:

$$\nabla.(-D\vec{\nabla}c + \vec{v}c) = \pm\dot{R}, \tag{4}$$

where D is the mass diffusivity, $\vec{v}$ is the velocity fields (m/s), c is the molar concentration (mol/l) and $\dot{R}$ is the reaction rate (mol/(l.s)). In the case of first order chemical reaction, one can model the reaction rate as $\dot{R} = k\prod_i c_i$, where k is the reaction rate coefficient (l/(mol.s)). Eq. (4) can be simplified under the following assumption: (i) Hele Shaw flow is assumed inside the channel where the velocity is uniform in the y direction far from the channel walls, i.e. $\vec{v} \approx v$ where $v = Q/(h_c l_c)$ is the mean velocity; (ii) the mass diffusivity is constant and depend only on the compound (NaOH or HCl); (iii) the reactants enters in the channel with the same molar concentration c_0; and (iv) the streamwise diffusion is neglectable compare to the convection. This latter assumption is derived from the Peclet number, defined as $\mathrm{Pe} = vl_c/D \gg 1$. Moreover, although the microfluidic channel works mostly in the so-called Taylor-Aris [30] regime where the parabolic velocity profile enhances the apparent diffusion coefficient in the flow direction, the streamwise diffusion term is still negligible compared to the transverse term, since the streamwise gradients are very weak. Following the previous assumptions, Eq. (4) leads to

$$\begin{aligned} v\frac{\partial c_A}{\partial x} - D\frac{\partial^2 c_A}{\partial y^2} &= -kc_Ac_B, \\ v\frac{\partial c_B}{\partial x} - D\frac{\partial^2 c_B}{\partial y^2} &= -kc_Ac_B. \end{aligned} \tag{5}$$

For the sake of clarity, Eq. (5) can be rewritten in dimensionless form using $\tilde{x} = x/l_c$, $\tilde{y} = y/l_c$ and $\tilde{c}_i = c_i/c_0$ where c_0 is the inlet reactant concentration, taken equal for the species A and B. This leads to this new system

$$\begin{aligned} \frac{\partial \tilde{c}_A}{\partial \tilde{x}} - \frac{1}{\mathrm{Pe}_A}\frac{\partial^2 \tilde{c}_A}{\partial \tilde{y}^2} &= -\mathrm{Da}\tilde{c}_A\tilde{c}_B, \\ \frac{\partial \tilde{c}_B}{\partial \tilde{x}} - \frac{1}{\mathrm{Pe}_B}\frac{\partial^2 \tilde{c}_B}{\partial \tilde{y}^2} &= -\mathrm{Da}\tilde{c}_A\tilde{c}_B, \end{aligned} \tag{6}$$

where Pe_A and Pe_B are the Peclet numbers related to the species A and B, and $\mathrm{Da} = kl_cc_0/v$ is the Damköhler number. Zero flux boundary conditions are used on channel walls and constant reactants initial conditions are used at the channel inlet, i.e. $\tilde{c}_{A,B}(0,\tilde{y}) = \Theta(\pm(y-0.5))$ where Θ is the Heaviside function. Finally, using the molar fraction conservation, i.e. $\sum_i \tilde{c}_i = 1$, the mole fraction of the product C is obtained as $\tilde{c}_c = \frac{1}{2}(1-\tilde{c}_A-\tilde{c}_B)$ in the case of the present reaction.

2.2.2. Analytical solutions

In Eq. (6), the Damköhler number is of the most interest in diffusion-reaction process as it compares the convective mass transport rate $\sim v/l_c$ to the reaction rate $\sim kc_0$. A large Damköhler ($Da \gg 1$) number indicates that the reaction is fully developed and the reactants and products mass diffusion dominates. Conversely, a rather small Damköhler number ($\mathrm{Da} \sim 1$) indicates that both the reaction and diffusion are competing in the reactor. Consequently, the mass transport characterization is preferentially done using a large Damköhler ($Da \gg 1$), whereas the reaction rate coefficient measurement has to be performed using a small Damköhler to ensure the highest sensitivity on the estimated parameters. The value of the Damköhler can be easily tuned by changing the reactants mass flow rate in the reactor.

In the large Damköhler regime, the reaction is fully developed which leads to $\tilde{c}_A\tilde{c}_B \sim 0$ close to the interface, i.e. at $\tilde{y} \sim 0.5$. Thus, outside the interface, between $0 < \tilde{y} < 0.4$ and $0.6 < \tilde{y} < 1$ for example, the source term vanishes, and the Eq. (6) are reduced to classical diffusion equations. Using the semi-infinite assumption (no influence of the channel side walls), and the boundary condition $\tilde{c}_{A,B}(\tilde{y}^*_{A,B}) = 0$, one can derive the following analytical solution for the species A and B [16]:

$$\tilde{c}_{A,B} = \mathrm{erf}\left(\pm\frac{\tilde{y}-\tilde{y}^*_{A,B}}{2\sqrt{\tilde{x}/\mathrm{Pe}_{A,B}}}\right), \tag{7}$$

where $\tilde{y}^*_{A,B}$ are constants linked to the position the reaction interface which can be different from 0.5 if the mass diffusivity of the species A and B are different [31] (which is the case in the NaOH and HCl reaction). Eq. (7) is used to fit the molar fraction fields and to estimate the mass diffusivity of each reactant.

Under the large mass flow rate in the reactor, the Damköhler is

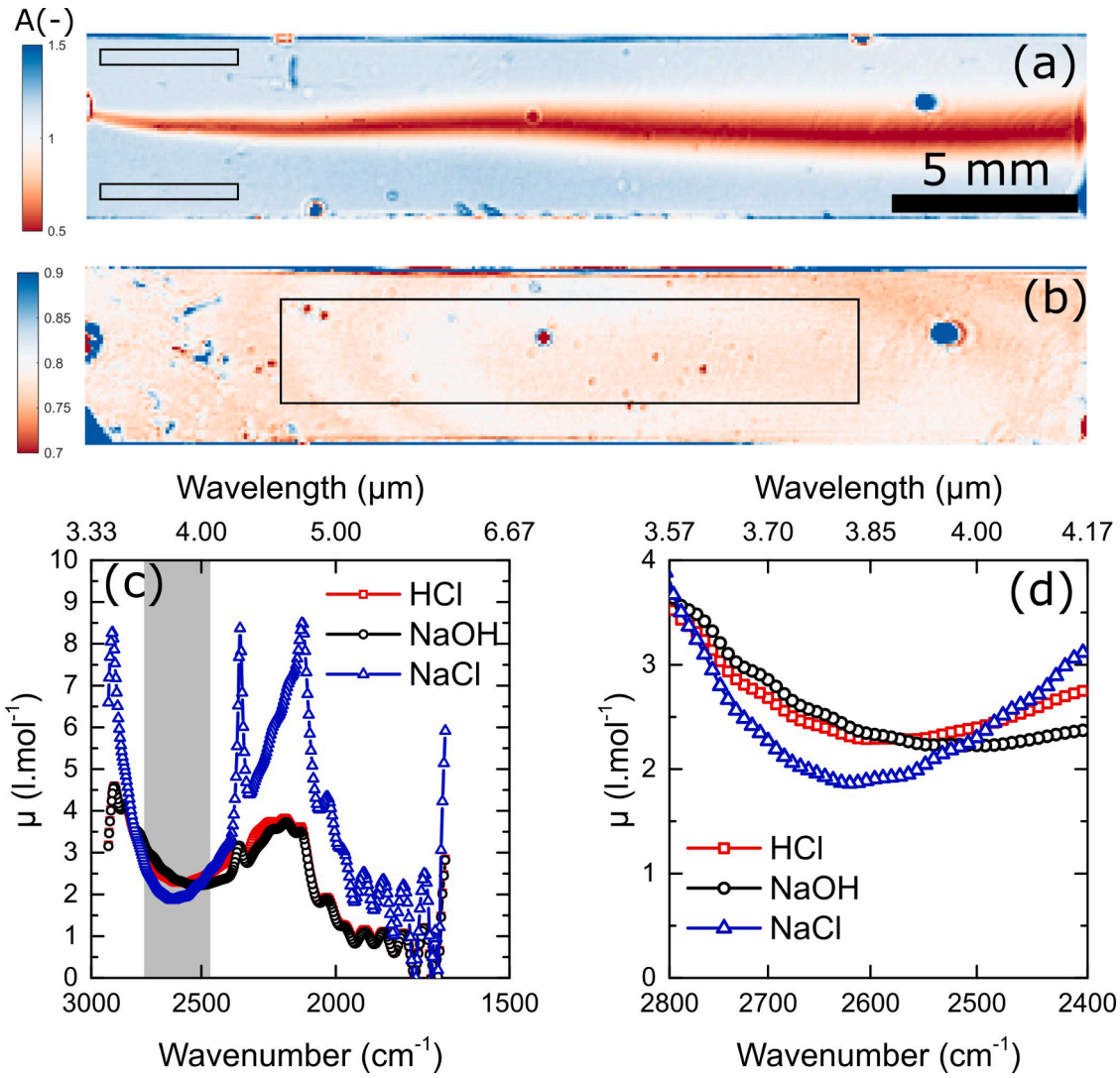

Fig. 3. Absorptivity coefficient measurements of the reactants and the product. Absorbance fields at 2600 cm^{-1} (a) of the chemical reaction and (b) of the pure NaCl solution. (c) Average absorptivity coefficient measured over the full spectral range; the gray area indicates the region of interest. (d) The cropped range of 2800–2400 cm^{-1} is used to compute the molar concentration.

relatively small and the reaction is not fully developed [12]. A semi-analytical solution to Eq. (6) was derived by Gálfi and Rácz [31] under semi-infinite regime and for Damköhler numbers of order of unity (named large time scale regime in their work [31]). In their work, the authors showed that the reaction rate at the interface scales as $\dot{R}^i = k\widetilde{c}_A^i\widetilde{c}_B^i \approx 0.298k(\pi \mathrm{Da}\widetilde{x})^{-2/3}$, the superscript i designating the reaction interface. This position is located, for all the $\widetilde{x}$ coordinates at the maximum salt concentration, $\widetilde{c}_C^i = \max(\widetilde{c}_C(\widetilde{x}))$.

Therefore, using the analytical result from Gálfi and Rácz [31], and considering that at the reaction interface, when $\widetilde{c}_C$ is maximum, the following property can be assumed: $\widetilde{c}_A^i \approx \widetilde{c}_B^i \approx \frac{1}{2} - \widetilde{c}_C^i$, so $\widetilde{c}_A^i\widetilde{c}_B^i \approx \left(\frac{1}{2} - \widetilde{c}_C^i\right)^2$. This results in a salt concentration at the interface that can only be solved in the case of a large Damkhöler number as

$$\widetilde{c}_C^i(\widetilde{x}) \approx \frac{1}{2} - 0.546(\pi \mathrm{Da}\widetilde{x})^{-1/3}. \quad (8)$$

In logscale and using the definition of the Damkhöler number, Eq. (8) is rewritten as $\log\left(\frac{1}{2} - \widetilde{c}_C^i\right) = -\frac{1}{3}\log\left(19.3\frac{c_0 l_c}{v}\widetilde{x}\right) - \frac{1}{3}\log k$ to obtain a linear relation. Thus, the mass transfer coefficient can be estimated directly from the intercept of a linear fit performed on the $\widetilde{c}_C^i$ measurements.

3. Results & discussion

3.1. Heat and mass transfer imaging

3.1.1. Molar concentrations fields

Prior to the molar concentration measurements, the absorptivity coefficient of each species in solution (NaOH, HCl, and NaCl) was carefully measured between 3000 and 1600 cm^{-1} with a 4 cm^{-1} spectral resolution. To do so, the absorbance of each pure chemical at a known concentration was obtained. Concerning NaOH and HCl, the 0.5 mol/l absorbance was obtained at the channel inlet and far from the reaction interface (see the black rectangles in Fig. 3(a)). Concerning NaCl, a pure solution of 0.25 mol/l of product was prepared, and the absorbance measured through the microfluidic channel (see Fig. 3(b)). Finally, the multispectral absorbance measured from each pixel inside the black rectangles in Fig. 3(a) and (b) was averaged and normalized to the reference concentration to obtain the absorptivity coefficients in Fig. 3 (c).

Although the whole spectral range of the absorptivity coefficient could be used, the limit of 2800 – 2400 cm^{-1} was chosen (see Fig. 3(d)).

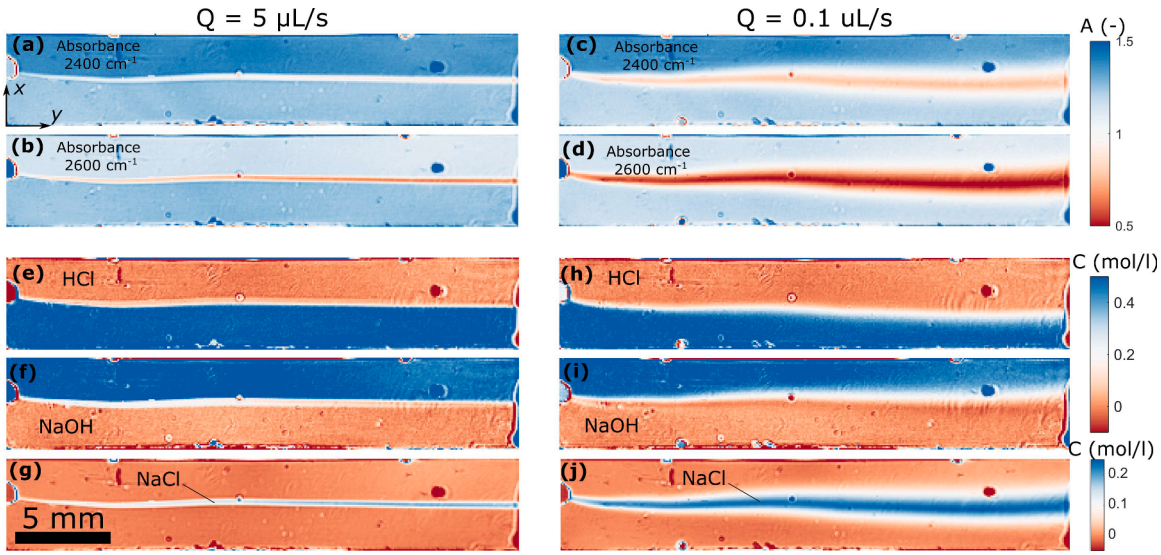

Fig. 4. Fields of absorbance for two wavenumbers, (a) to (d), and molar concentration, (e) to (j), measured for two flow rates 5 and 0.1 µl/s. The channel inlet is located on the left.

This specific range presents the advantage of having a relatively low absorption, which ensures a higher signal-to-noise ratio during the measurements. In addition, NaOH and HCl show no correlation over this range, i.e. they present a different spectral signature, which avoids any singularity in Eq. (3).

Once the calibration of the absorption coefficient done, the multi-spectral absorbances are measured following the methodology described in Ref. [27]. They are measured at four flow rates, i.e. 0.05, 0.1, 5 and 10 µl/s, to make the Damköhler number range through two orders of magnitude. Such operating conditions correspond to Peclet numbers ranging from 100 to 50, and a Damköhler ranging from 3 to 500, satisfying the assumptions made to derive the equations presented in the model Section 2.2.2.

Fig. 4 presents the measurements performed at two flow rates, where the absorbances for two wavenumbers are shown (see Fig. 4(a) to (d)). These fields are converted into molar concentration using Eq. (3) and the absorption coefficient previously measured in Fig. 3. A linear regression based on Eq. (3) is performed to obtain the concentration of each species and the associated standard deviation using the spectrum between 2800 cm^{-1} and 2400 cm^{-1}.

In Fig. 4(e) to (j), the HCl, NaOH and NaCl molar concentration fields are presented. The concentrations of HCl and NaOH are observed to decrease near the reaction interface whereas the concentration of NaCl was observed to increase from the inlet (left) to the outlet (right) along the channel. Such behavior is similar to the ones reported in the literature using the same acid/base reaction [25]. It is also observed that the range of the molar concentration is between 0 and 0.5 mol/l for HCl and NaOH and between 0 and 0.25 mol/l for NaCl, validating the molar concentration measurements.

Small stains are visible in all the absorbance and concentration fields in Figs. 3 and 4, which are mainly due to small imperfections in the camera and beam expander optics as well as in the plane mirrors used in our experimental setup. However, these imperfections do not affect the concentrations fields; they only add local uncertainty to the images. Small hydrodynamic instabilities in the channel are also visible. It indicates that the channel may not have been small enough to ensure Hele Shaw flow. A thinner channel would have been better to stabilize the flow, and would improve upon the presented measurements. Nevertheless, this does not impact the results, as the measurement of the concentration fields is still possible despite the small hydrodynamics instabilities.

In Fig. 4, it is also interesting to note the effect of the flow rate on the concentration fields. At high flow rates, i.e. 5 µl/s, only the onset of the reaction is visible in the channel as the residence time, $\tau_R \sim l_c/v$, is very short, i.e. of the order of 500 ms. Thus, in this case, it is possible to study the acid/base reaction when the reactants have just started to react and therefore characterizing the mass transfer. In contrast, at low flow rates, i.e. 0.1 µl/s, the long residence time (> 100 s) ensures complete mixing between the reactants where the diffusion of the product is largely developed. These two effects are needed to characterize both mass transport and transfer rates as indicated in Section 2.2.2.

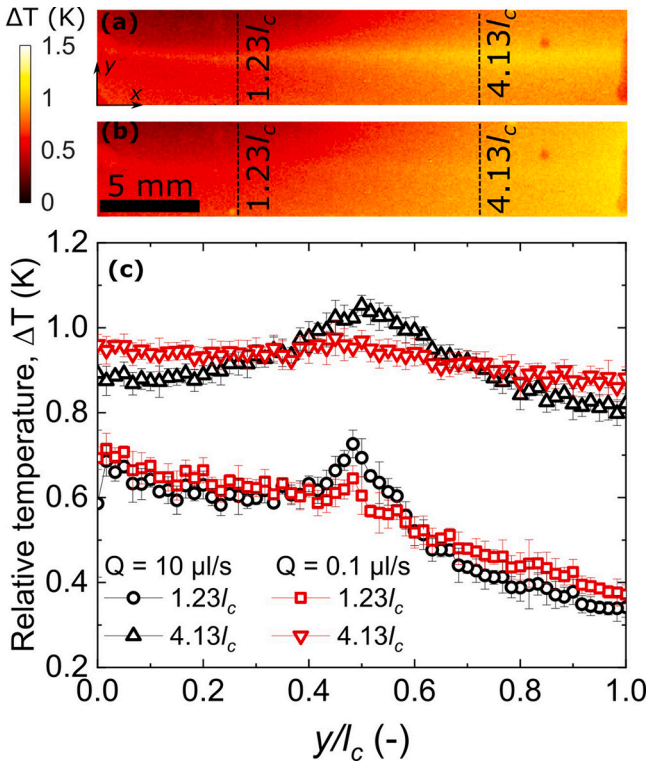

Fig. 5. Temperature fields measured at 10 µl/s (a) and 0,1 µl/s (b). (c), Profiles of relative temperature for two flow rates at two x-positions indicated by the dash lines in (a) and (b).

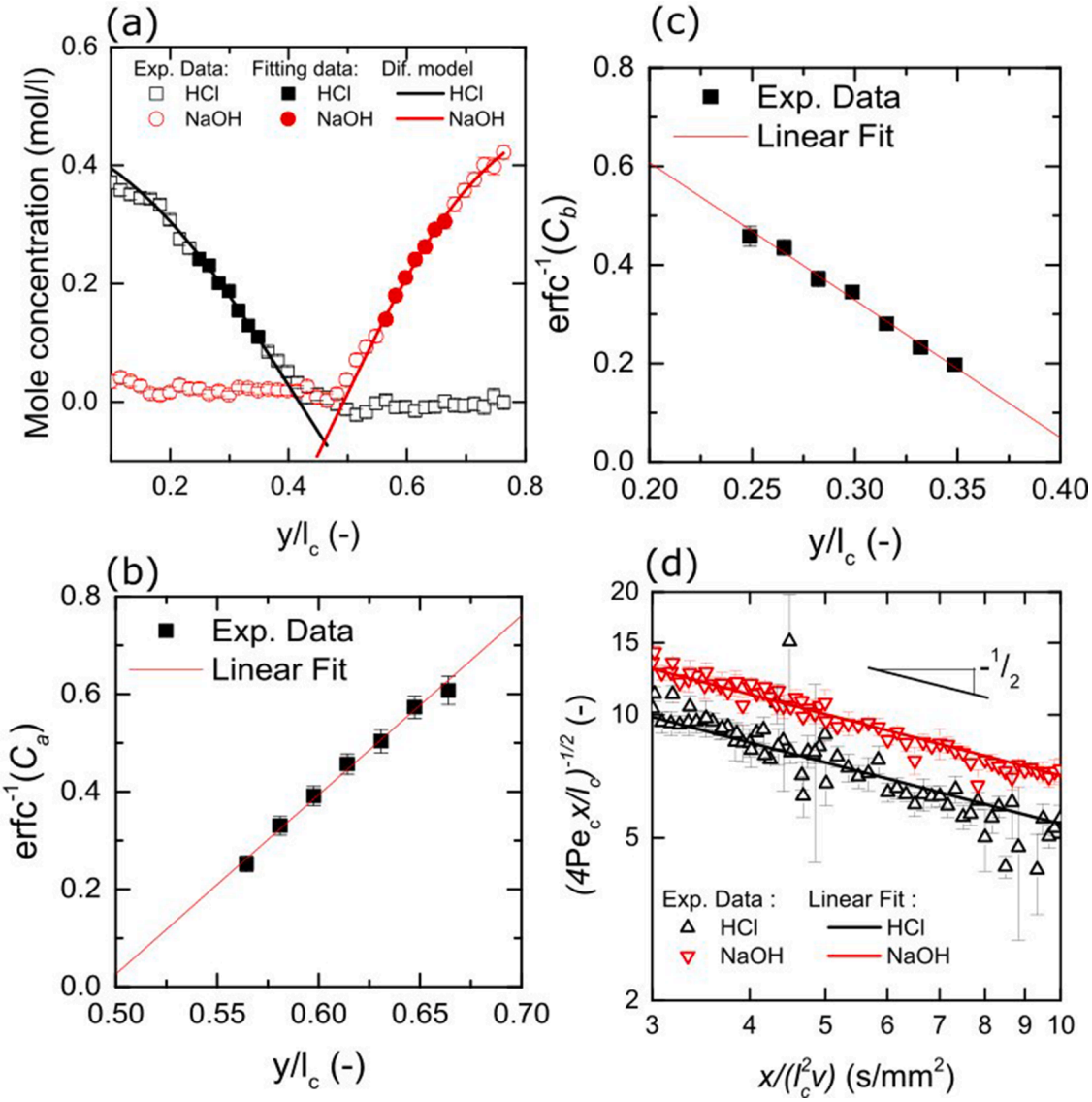

Fig. 6. Estimation of reactants and product mass diffusivity. (a) NaOH and HCl molar concentration at $\tilde{x} = l_c$ and $Q = 0.05$ µl/s. The solid symbols indicate the data chosen for the linear fit, and the solid line is the diffusive model (Eq. (7)). (b) and (c), linear fit of the diffusive model for NaOH and HCl, respectively. (d), Second linear fit from which the mass diffusivity is obtained.

3.1.2. Temperature fields

The heat fields are measured for all the flow rates, but only the results obtained at 10 and 0,1 µl/s are presented in Fig. 5(a) and (b). The relative temperature rising due to the reaction is very small (less than 1 K at the maximum) which justifies the use of very sensitive and cooled IR cameras. The typical noise of the measured temperature is observed to be around 0.1 K.

At high flow rates (Fig. 5(a)) a clear heat source is observed at the middle of the sample corresponding to the zone where the chemicals are reacting (see Fig. 4(g) for comparison). It can be noticed that the heat diffusion zone is much larger than the one from the mass diffusion at 5 µl/s. This is due to the larger heat diffusivity (typically around 10^{-7} m^2/s for water) compared to the mass diffusivity (in the order of 10^{-9} m^2/s for liquids, see next section). This is confirmed in Fig. 5(b) where the flow become completely isothermal whereas the species have not diffused up to the channel side walls at the same flow rate (see Fig. 4(j) for comparison). This result can also be explained in terms of Peclet numbers: the heat and mass diffusion zone would have the same size if the thermal and mass Peclet numbers are equal. In the case of thermal transport at 5 µl/s, the Peclet is about $Pe_T = vl_c/a \approx 10^2$ which is relatively low. In contrast, the Peclet number associated with the mass transport is around 10^4. Thus, by using a flow rate a hundred time faster for thermal measurements than for the molar concentration measurements, one can obtain a similar diffusion pattern [25].

A deeper analysis of the thermal profiles is carried out through the Fig. 5(c). For each flow rate, the *y*-profiles are extracted for two channel positions (one closest to the inlet and the other closest to the outlet). At 10 µl/s, a clear temperature peak is visible in the middle of the channel indicating the presence of the heat source from the chemical reaction. However, a lateral gradient is also visible in the flow in the *y*-direction. This thermal gradient is due to an extra chemical reaction at the NaOH interface with the dry film photopolymer used to build the microfluidic chip. Such reaction with NaOH was not mentioned by the photopolymer film supplier. Although, it was invisible through the IR spectroscopy analysis, it has been clearly revealed using the highly sensitive IR camera in this study. Nevertheless, this extra reaction is located far from the NaOH/HCl interface, and therefore does not impact the acid/base reaction nor the NaCl production rate. Finally, this result illustrates the strength of the thermospectroscopic method for visualizing the chemical process that takes place in a microfluidic reactor through both mass and

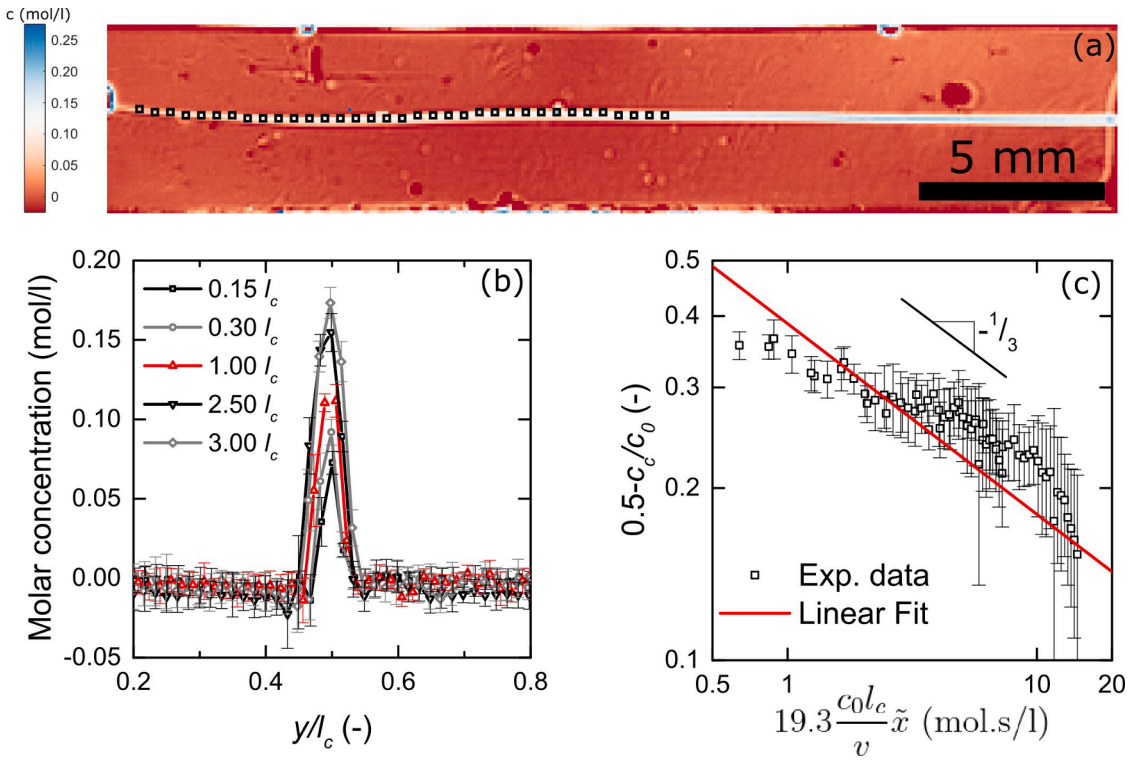

Fig. 7. Measurements of the reaction rate coefficient. (a) NaCl molar concentration fields measured at 5 µ/l. The black squares indicate the chosen data at the reaction interface. (b) NaCl molar distribution profiles for selected channel positions. (c), linear fit in log-scale of the reaction rate coefficient.

heat fields. This technique can be extended to any exo- or endothermic reaction with the same ability to distinguish the heat and mass transfer (heat transfer remain a continuous component in the spectroscopic measurements).

3.2. Comparison with the reactor model

3.2.1. Binary mass diffusivity estimations

The concentration fields measured at 0.1 and 0.05 µl/s are used to estimate the binary mass diffusivity of NaCl/NaOH and NaCl/HCl. Only the concentration fields from NaOH and HCl are used, but the study could also have been done using the concentration fields of NaCl.

Eq. (7) is fitted to the measurements to obtain the mass diffusivity. The fitting of this equation was realized in two steps, following a methodology similar to Salmon et al. [16]. At each x-position in the channel, a linear fit was performed, i.e. $\mathrm{erf}^{-1}\tilde{c}_{A,B} = A(\tilde{x})\tilde{y} + B(\tilde{x})$ where $A(\tilde{x}) = (2\sqrt{\tilde{x}/\mathrm{Pe}_{A,B}})^{-1}$ and $B(\tilde{x}) = \tilde{y}^{*}(2\sqrt{\tilde{x}/\mathrm{Pe}_{A,B}})^{-1}$. Such linear fits were done outside of the reaction interface, and far from the walls to ensure the semi-infinite assumption. In Fig. 6(a), the concentration profiles of NaOH and HCl are presented at one channel position. Only the solid symbols were taken to perform the linear fit. All the linear fits were performed at $\tilde{x} \in [l_c\,; 4l_c]$. To illustrate this, Fig. 6(b) and (c) show the linear fits performed at $\tilde{x} = l_c$.

Once the values of $A(\tilde{x})$ are obtained for all the channel positions at 0.1 and 0.05 µl/s, a second linear fit is performed in log-scale to obtain the mass diffusivity, i.e. $\log(2A(\tilde{x})) = -\frac{1}{2}\log D - \frac{1}{2}\log(\tilde{x}/(l_c v))$. Thus $2A(\tilde{x})$ is plotted versus $\tilde{x}/(l_c v)$, and the value of the intercept gives the mass diffusivity. In this fitting procedure, the slope $-\frac{1}{2}$ was fixed, and only the value of the intercept was estimated.

Fig. 6(d) shows all the data point used in the fitting procedure. By comparing the model (solid line) to the experimental data (symbols), it can be observed that the data follows the slope $-\frac{1}{2}$ well, exhibiting the diffusive nature of the mass transport in the channel y-direction. This first result validates the assumptions proposed to model the reactor, and the quality of the measurements made to estimate the mass diffusivity.

For each compound, the value of the mass diffusivity is computed from the intercept of the linear fit. It was found that $D_A = (2.0 \pm 0.1) \times 10^{-3}$ mm^2/s and $D_B = (3.4 \pm 0.2) \times 10^{-3}$ mm^2/s for NaCl/NaOH and NaCl/HCl, respectively. The uncertainty comes from the standard deviation of the intercept computed with a 99% confidence interval using the Student Law [32]. These values are typically in the range reported by other studies, such as in [33] using an imaging method, or in [34] using Rayleigh interferometry to measure the diffusion of NaCl in water. Compared to the traditional stopped-flow method [15] used to measure the mass diffusivities, the proposed methodology ensures a rapid and in operando method suitable for online characterizations.

3.2.2. Reaction rate coefficient estimation

The NaCl concentration field measurements, depicted in Fig. 7(a) at 10 and 5 µl/s, were used to measure the mass transfer rate through the value of the reaction rate coefficient. It is observed that the NaCl concentrates only at the NaOH/HCl interface, and it is close to zero everywhere else in the channel. Although a slight uncertainty of ± 10% is observed in some area of the channel. Some hydrodynamic instabilities are also observed at these high flowrates which may be due to the onset of stronger inertia forces in the flow compared to the low flowrates, and/or the presence of small pressure oscillations in the syringe pump. Decreasing the size of the reactor would solve this issue [35].

At high flow rates, it is found that the NaOH and HCl reaction is not fully completed. This result is evidenced through the NaCl concentration profiles in Fig. 7(b) where the molar concentration at the reaction interface did not reach the 0.25 mol/l limit and kept increasing in the x-direction. In theory, the intrinsic reaction rate coefficient is in the order of 10^9 l/mol/s for the NaOH/HCl reaction, leading to mass transfer in the order of $\tau = (kc_0)^{-1} \sim 1$ ns [26]. With the channel geometry and flow rate used in this study, a maximum residence time in the order of 500 ms can be reached, indicating that the NaOH/HCl reaction should be fully completed, and a concentration of 0.25 mol/l of NaCl would

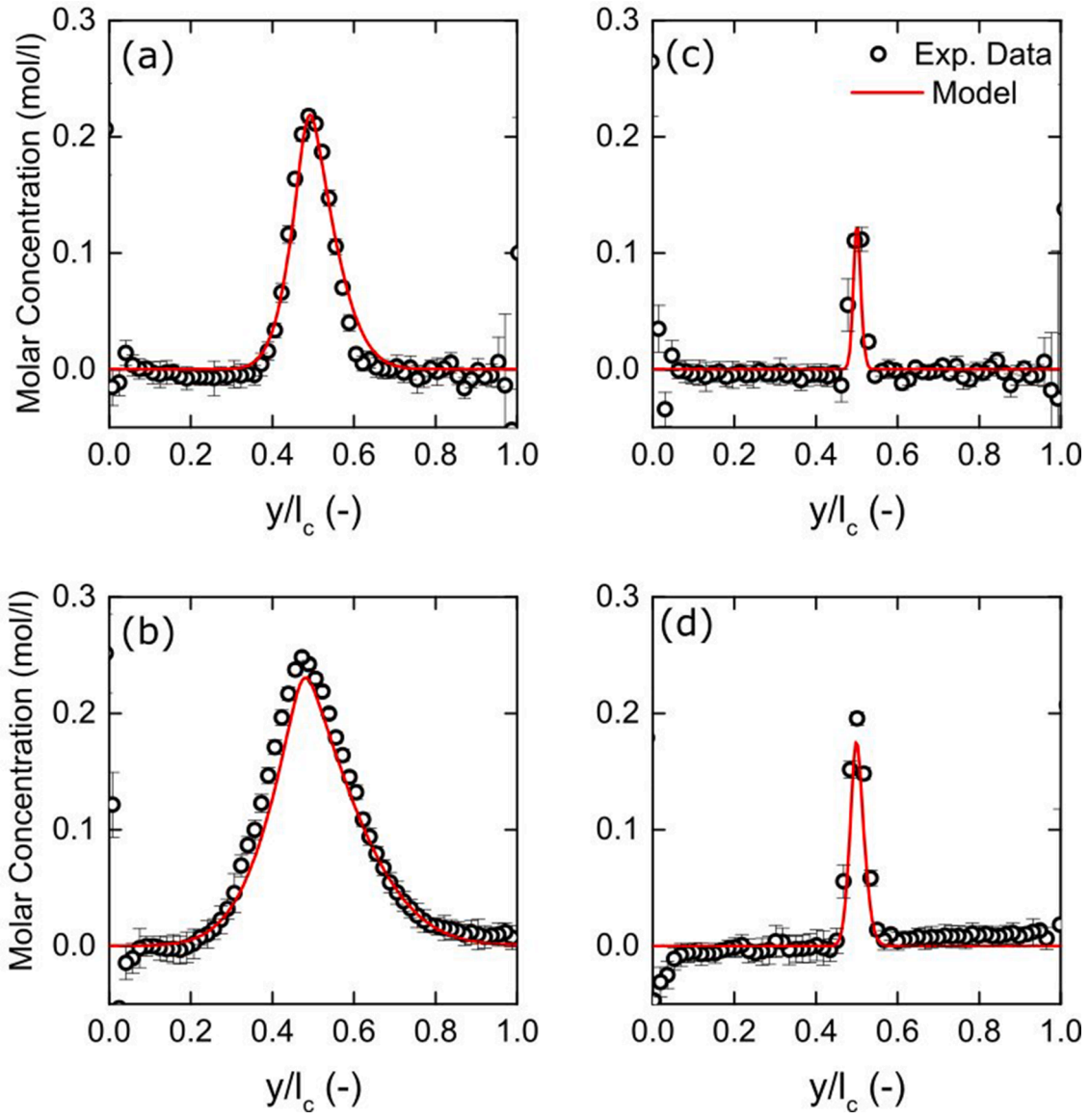

Fig. 8. NaCl molar concentration profiles. Comparison of the measurements and the numerical model for $Q = 0.1$ µl/s, (a) and (b), and for $Q = 5$ µl/s, (c) and (d). Data is presented for two channel positions, $\tilde{x} = l_c$ (top) and $\tilde{x} = 4l_c$ (bottom). Model physical parameters are taken from the previous estimation, i.e. $D_B = 3.4 \times 10^{-3}$ mm^2/s, $D_A = 2.0 \times 10^{-3}$ mm^2/s and $k = 17$ l/mol/s.

have been measured at the interface everywhere in the channel. Thus, the result obtained in Fig. 7(b) evidence the diffusion limiting regime of the reaction in such laminar microfluidic reactors, leading to a slower than expected mass transfer rate in the order of hundreds of milliseconds.

The methodology used to measure the reaction rate coefficient, k, was derived from the analytical solution of the advection-diffusion-reaction (Eq. (6)) reported by Gálfi and Rácz [31] and was detailed in the Section 2.2.2. The concentration of NaCl at the interface was extracted for $\tilde{x} \in [0.15l_c\ ; 3l_c]$ from the image (see black squares in Fig. 7 (a)) and presented in log-scale versus $19.3l_c c_0 x/v$. A linear fit with a fixed slope of $-\frac{1}{3}$ was performed on the data to estimate the intercept. As expected, the data globally followed the $-\frac{1}{3}$ slope even though few data points are outside the linear model. These deviations are mainly explained from the high flow rate used to carry out these measurements where some hydrodynamic instabilities may occur [3], as pointed out earlier. The reaction interface moves slightly during the 8 s needed to record an interferogram which have blurred the exact position of the interface and introduced some uncertainties in the NaCl concentration measurements.

From the linear fit in Fig. 7(c), the value of the intercept is obtained and used to compute the reaction rate coefficient. A value of $k = 17 \pm 5$ l/mol/s with a 99.9% confidence interval was obtained in this study. Such value is significantly lower than the intrinsic NaOH/HCl reaction rate coefficient due to the presence of the diffusion-limited regime in such laminar microfluidic reactor. A different reaction rate would be measured in a different microfluidic reactor geometry, i.e. a thinner channel would likely increase the reactant diffusion and therefore enhance the mass transfer rate. For example, Kise et al. [19] stated that the mixing time is strongly dependent on the diffusion time and can get down several orders of magnitude. Asano and Togashi [36] reported a similar observation where in dilute solutions the observed reaction rates can be several orders of magnitude slower than the intrinsic or absolute rate coefficient.

3.2.3. *Validation of the method*

To validate the method, a comparison of the NaCl molar concentration profiles measured at two channel positions and flow rates is

made versus the model (Eq. (6)) using the binary mass diffusivities and reaction rates measured in Sections 3.2.1 and 3.2.2. Eq. (6) is solved numerically using a finite difference method in the y-direction and the Runge-Kutta algorithm in the x-direction. The concentrations of NaOH and HCl are computed to obtain the concentration of NaCl through mass conservation.

Fig. 8 shows the comparison between the numerical model and the molar concentration profiles measured at two flow rates and two channel positions. Overall, an excellent agreement between the measurements and the numerical results is observed. In Fig. 8(a) and (b), the low flow rate used highlights the effect of NaCl diffusion at the inlet and at the middle of the channel, respectively. The asymmetry of the NaCl diffusion profiles comes from the higher mass diffusivity of NaCl/HCl compared to NaCl/NaOH. At high flow rates, Fig. 8(c) and (d), the effect of the mass transfer is highlighted. The model agrees well with the measurements, but a small deviation is observed at $\tilde{x} = 4l_c$ (Fig. 7(d)). The NaCl concentration at the interface is slightly underestimated meaning than the reaction rate coefficient could also be underestimated. This effect is also observed in Fig. 7(b). Nevertheless, the in operando characterization of the mass transport and transfer rates realized in this study enables accurate prediction of the microfluidic reactor behavior, validating the complete analytical method proposed in this work. This illustrates the quantitative aspect of the data measured using the thermospectroscopic imaging method. This data can be used to get a better understanding of the reaction through the physical parameters governing the mass transfer and to feed artificial intelligence algorithms, which can help in the design of more efficient microfluidic reactor.

4. Conclusions

In this work, a novel imaging technique applied to microfluidic flows was developed. It enabled simultaneous measurement of the heat and mass fields of a chemical reaction. This technique is based on a unique combination of a FTIR spectrometer with an IR camera, which ensures high sensitivity of the sensor, i.e. it enables detection of an IR beam through 100 μm of water. Moreover, complete images of all the chemical molar concentrations and the associated heat fields were obtained every 8 s which opens the path toward online monitoring or product screening for the industry. Therefore, this new technique is an additional toolbox for chemists to characterize and control reactions in microfluidic reactors. The only drawback at this moment is the somewhat limited spectral range (4000–1700 cm^{-1}) compared to the range offered by commercial FTIR, but this range can be adjusted by changing the IR camera, as already performed in a previous study [27]. In addition, the current pixel size of 83 μm can also be improved by using a microscope objective lens to decrease the spatial resolution down to 10 μm, opening the door toward smaller microfluidic channels.

The quantitative aspect of the data obtained through thermospectroscopic imaging was also studied by comparing the data to a simple reactor model. The mass transport and transfer rates were measured using an analytical inverse processing method. The binary mass diffusivities of NaCl/HCl and NaCl/NaOH were measured typically in the range reported by other studies in literature using the stopped-flow technique. The reaction rate coefficients were found to be several orders of magnitude lower than the intrinsic NaOH/HCl one, evidencing the presence of a diffusion-limited regime in the microfluidic reactor. These results enable the separation of physics from chemistry to get a better understanding of the reaction, assessment of the reactor quality, quantification of the reaction efficiency and fine-tuning of the reaction. The good agreement observed between the reactor model and our experimental data shows that the mass transfer physics of the reaction were fully understood.

Last but not the least, the methodology was presented in the paper using 2 reactants and 1 product, but it can be extended to any similar reaction. The next step is to master heat transfer in the reaction with the appropriate model and reactor design improvement to pave the way toward advanced in operando, online and contactless calorimetry methods.

Declaration of Competing Interest

The authors declare that they have no known competing financial interests or personal relationships that could have appeared to influence the work reported in this paper.

Acknowledgments

ADEME is gratefully acknowledged by the authors for its support through the project IGAR. The authors would also acknowledge Mrs Lucie Lindingre and Mr Gérald Clisson for their technical assistance during this work. S.C. gratefully acknowledges the French National Research Agency (ANR) for its support through the project I2MPAC (ANR-20-CE05-0018). Mr. K. Krause is also gratefully acknowledged for its valuable help during the manuscript preparation.

References

[1] G.M. Whitesides, The origins and the future of microfluidics, Nature 442 (2006) 368–373, https://doi.org/10.1038/nature05058.
[2] A.J. DeMello, Control and detection of chemical reactions in microfluidic systems, Nature 442 (2006) 394–402, https://doi.org/10.1038/nature05062.
[3] H.A. Stone, A.D. Stroock, A. Ajdari, Engineering flows in small devices: microfluidics toward a lab-on-a-chip, Annu. Rev. Fluid Mech. 36 (2004) 381–411, https://doi.org/10.1146/annurev.fluid.36.050802.122124.
[4] H.T. Zhao, Y. Zhang, P.Y. Liu, P.H. Yap, W. Ser, A.Q. Liu, Chemical reaction monitoring via the light focusing in optofluidic waveguides, Sens. Actuators B Chem. 280 (2019) 16–23, https://doi.org/10.1016/j.snb.2018.10.048.
[5] P. Hinsmann, J. Frank, P. Svasek, M. Harasek, B. Lendl, Design, simulation and application of a new micromixing device for time resolved infrared spectroscopy of chemical reactions in solution, Lab Chip 1 (2001) 16, https://doi.org/10.1039/b104391a.
[6] S. Seibt, P. Mulvaney, S. Förster, Millisecond CdS nanocrystal nucleation and growth studied by microfluidics with *in situ* spectroscopy, Colloids Surf. A Physicochem. Eng. Asp. 562 (2019) 263–269, https://doi.org/10.1016/j.colsurfa.2018.10.043.
[7] A. Abou-Hassan, O. Sandre, V. Cabuil, Microfluidics in inorganic chemistry, Angew. Chem. Int. Ed. 49 (2010) 6268–6286, https://doi.org/10.1002/anie.200904285.
[8] F. Sarrazin, L. Prat, N. Di Miceli, G. Cristobal, D.R. Link, D.A. Weitz, Mixing characterization inside microdroplets engineered on a microcoalescer, Chem. Eng. Sci. 62 (2007) 1042–1048, https://doi.org/10.1016/j.ces.2006.10.013.
[9] C. Pradere, M. Joanicot, J.C. Batsale, J. Toutain, C. Gourdon, Processing of temperature field in chemical microreactors with infrared thermography, Quant. Infrared Thermogr. J. 3 (2006) 117–135, https://doi.org/10.3166/qirt.3.117-135.
[10] M. Romano, C. Pradere, F. Sarrazin, J. Toutain, J.C. Batsale, Enthalpy, kinetics and mixing characterization in droplet-flow millifluidic device by infrared thermography, Chem. Eng. J. 273 (2015) 325–332, https://doi.org/10.1016/j.cej.2015.03.071.
[11] T. Gavoille, N. Pannacci, G. Bergeot, C. Marliere, S. Marre, Microfluidic approaches for accessing thermophysical properties of fluid systems, React. Chem. Eng. 4 (2019) 1721–1739, https://doi.org/10.1039/C9RE00130A.
[12] J.B. Salmon, C. Dubrocq, P. Tabeling, S. Charier, D. Alcor, L. Jullien, F. Ferrage, An approach to extract rate constants from reaction−diffusion dynamics in a microchannel, Anal. Chem. 77 (2005) 3417–3424, https://doi.org/10.1021/ac0500838.
[13] A.M. Huebner, C. Abell, W.T.S. Huck, C.N. Baroud, F. Hollfelder, Monitoring a reaction at submillisecond resolution in picoliter volumes, Anal. Chem. 83 (2011) 1462–1468, https://doi.org/10.1021/ac103234a.
[14] C.N. Baroud, F. Okkels, L. Ménétrier, P. Tabeling, Reaction-diffusion dynamics: confrontation between theory and experiment in a microfluidic reactor, Phys. Rev. E 67 (2003), 060104, https://doi.org/10.1103/PhysRevE.67.060104.
[15] A.E. Kamholz, B.H. Weigl, B.A. Finlayson, P. Yager, Quantitative analysis of molecular interaction in a microfluidic channel: the T-sensor, Anal. Chem. 71 (1999) 5340–5347, https://doi.org/10.1021/ac990504j.
[16] J.B. Salmon, A. Ajdari, P. Tabeling, L. Servant, D. Talaga, M. Joanicot, *In situ* Raman imaging of interdiffusion in a microchannel, Appl. Phys. Lett. 86 (2005), 094106, https://doi.org/10.1063/1.1873050.
[17] F. Sarrazin, J.B. Salmon, D. Talaga, L. Servant, Chemical reaction imaging within microfluidic devices using confocal Raman spectroscopy: the case of water and deuterium oxide as a model system, Anal. Chem. 80 (2008) 1689–1695, https://doi.org/10.1021/ac7020147.
[18] Y. Lin, X. Yu, Z. Wang, S.T. Tu, Z. Wang, Measurement of temperature-dependent diffusion coefficients using a confocal Raman microscope with microfluidic chips considering laser-induced heating effect, Anal. Chim. Acta 667 (2010) 103–112, https://doi.org/10.1016/j.aca.2010.03.061.

[19] D.P. Kise, D. Magana, M.J. Reddish, R.B. Dyer, Submillisecond mixing in a continuous-flow, microfluidic mixer utilizing mid-infrared hyperspectral imaging detection, Lab Chip 14 (2014) 584–591, https://doi.org/10.1039/c3lc51171e.
[20] M. Ryu, J.A. Kimber, T. Sato, R. Nakatani, T. Hayakawa, M. Romano, C. Pradere, A. A. Hovhannisyan, S.G. Kazarian, J. Morikawa, Infrared thermo-spectroscopic imaging of styrene radical polymerization in microfluidics, Chem. Eng. J. 324 (2017) 259–265, https://doi.org/10.1016/j.cej.2017.05.001.
[21] K.L.A. Chan, S. Gulati, J.B. Edel, A.J. de Mello, S.G. Kazarian, Chemical imaging of microfluidic flows using ATR-FTIR spectroscopy, Lab Chip 9 (2009) 2909, https://doi.org/10.1039/b909573j.
[22] A. Perro, G. Lebourdon, S. Henry, S. Lecomte, L. Servant, S. Marre, Combining microfluidics and FT-IR spectroscopy: towards spatially resolved information on chemical processes, React. Chem. Eng. 1 (2016) 577–594, https://doi.org/10.1039/C6RE00127K.
[23] K.L.A. Chan, S.G. Kazarian, FT-IR spectroscopic imaging of reactions in multiphase flow in microfluidic channels, Anal. Chem. 84 (2012) 4052–4056, https://doi.org/10.1021/ac300019m.
[24] M. Lehtihet, E. Abisset, S. Chevalier, A. Sommier, C. Pradere, J. Leng, Thermospectroscopic infrared imaging of a confined drying process, Chem. Eng. J. 403 (2021), 126167, https://doi.org/10.1016/j.cej.2020.126167.
[25] T. Uema, T. Ohata, Y. Washizuka, R. Nakanishi, D. Kawashima, N. Kakuta, Near-infrared imaging in a microfluidic channel of aqueous acid–base reactions, Chem. Eng. J. 403 (2021), 126338, https://doi.org/10.1016/j.cej.2020.126338.
[26] E. Pines, B.Z. Magnes, M.J. Lang, G.R. Fleming, Direct measurement of intrinsic proton transfer rates in diffusion-controlled reactions, Chem. Phys. Lett. 281 (1997) 413–420, https://doi.org/10.1016/S0009-2614(97)01245-1.
[27] S. Chevalier, J.N. Tourvieille, A. Sommier, J.C. Batsale, B. Beccard, C. Pradère, Thermal camera-based fourier transform infrared thermospectroscopic imager, Appl. Spectrosc. 75 (2021) 462–474, https://doi.org/10.1177/0003702820973026.
[28] A. Aouali, S. Chevalier, A. Sommier, E. Abisset-Chavanne, J.C. Batsale, C. Pradere, 3D infrared thermospectroscopic imaging, Sci. Rep. 10 (2020) 22310, https://doi.org/10.1038/s41598-020-78887-x.
[29] R.G. Brereton, Introduction to multivariate calibration in analytical chemistry, Analyst 125 (2000) 2125–2154, https://doi.org/10.1039/b003805i.
[30] M. Pagitsas, A. Nadim, H. Brenner, Multiple time scale analysis of macrotransport processes, Phys. A Stat. Mech. Appl. 135 (1986) 533–550, https://doi.org/10.1016/0378-4371(86)90158-5.
[31] L. Gálfi, Z. Rácz, Properties of the reaction front in an A+B = C type reaction-diffusion process, Phys. Rev. A 38 (1988) 3151–3154, https://doi.org/10.1103/PhysRevA.38.3151.
[32] J.B. Kennedy, A.M. Neville, Basic Statistical Methods For Engineers and Scientists, Harper & Row, 1986. https://books.google.ca/books?id=8DUfAQAAIAAJ.
[33] K. Miyamoto, H. Ichimura, T. Wagner, M.J. Schöning, T. Yoshinobu, Chemical imaging of the concentration profile of ion diffusion in a microfluidic channel, Sens. Actuators B Chem. 189 (2013) 240–245, https://doi.org/10.1016/j.snb.2013.04.057.
[34] J.A. Rard, D.G. Miller, The mutual diffusion coefficients of NaCl-H_2O and $CaCl_2$-H_2O at 25°C from Rayleigh interferometry, J. Solut. Chem. 8 (1979) 701–716, https://doi.org/10.1007/BF00648776.
[35] P. Tabeling, Introduction to microfluidics, 2005.
[36] Y. Asano, S. Togashi, A study of solvent effects on reaction rates using a microreactor, J. Chem. Eng. Japan 43 (2010) 798–809, https://doi.org/10.1252/jcej.09we240.